Research Article

Spot-Centroid Determination Algorithms in Semiactive Laser Photodiodes for Artillery Applications

Raul de Celis [iD] **and Luis Cadarso** [iD]

European Institute for Aviation Training and Accreditation (EIATA), Rey Juan Carlos University, Fuenlabrada, Madrid, 28943, Spain

Correspondence should be addressed to Raul de Celis; raul.decelis@urjc.es

Precision of guided projectiles depends equally on the accuracy in determining the coordinates of the objective and on the exactness of the measurement devices utilized for position and attitude calculation of the projectile. Development of algorithms for low-cost high-precision terminal guidance systems is a cornerstone in research in this field. Semiactive laser (SAL) kits, and particularly quadrant detector devices, have been developed to improve precision in guided weapons. Photodetection system can be functionally divided into two main parts: sensing and processing. The sensed signal is processed to estimate the spot coordinates, i.e., the laser footprint, which provides some information regarding projectile-target relative position, to obtain the needed information for the navigation and guidance algorithms. The electrical intensities that a real sensor provides under laboratory conditions are compared to a mathematical model based on area intersection calculations to simulate the intensities on real flights. Then, four different processing algorithms, two of them rational, and the other two logarithmic, are tested for different spot sizes, which are nonlinear. Proposing an interpolation algorithm based on the four electrical intensities obtained in a semiactive laser quadrant photodetector, laser footprint center estimation is improved for artillery applications. Finally, an example illustrating a projectile flight is employed to compare real and calculated laser footprints in order to select the best algorithm for artillery applications.

1. Introduction

A guided ammo designed to hit a preassigned target and, in addition, to avoid or eliminate collateral damage is commonly denominated as a precision-guided munition (PGM). Since the destructive power of explosive weapons diminish with separation, even small enhancements in exactness permit an objective to be destroyed with less or smaller bombs. The accuracy of these weapons is needy both on the precision in setting the coordinates of the target and on the exactness of the position and attitude estimations of the measurement equipment utilized. Inertial measurement unit (IMU) and global navigation satellite system (GNSS) hybrid devices stretch the exact solutions for PGMs, yet in a few events, these arrangements probably will not be sufficient.

For those frameworks, a circular error probable (CEP) is around 10-20 m in the best cases [1]. Improvement of algorithms for minimal cost effort in high-accuracy terminal guidance devices has been the cornerstone in research on PGMs for the most recent years. Inertial sensor innovation is usually applied in applications nowadays [2]. A robust guidance algorithm, basically reasonable for devices typified by slight glint levels, for example, electrooptical munitions, is proposed by [3]. Another accuracy guidance law for 3-dimensional interceptions is presented in [4]. Rather than announced beforehand guidance algorithms, it does not require calculating the distance to the objective. This fact makes it fit for use on devices which have an imaging gadget, for example, a camcorder, as an essential sensor. Target determination is likewise an issue that must be considered;

[5] proposes a novel multitarget detection technique to distinguish nearby or firmly dispersed small infrared targets. A method for numerous objective detection is exhibited in [6].

Semiactive laser (SAL) kits, and especially quadrant detector gadgets, have been produced with the end goal of enhancing accuracy in guided weapons and also for recognizing multiple objectives. Quadrant photodetectors have been applied in a wide range of engineering areas, for example, in measurement [7, 8], laser collimation, control, angular encoder target tracking [9], and in particular in terminal guidance for PGMs [10, 11]. One of the best points of interest of quadrant detector hardware is the superior performance regarding guidance, ordinarily in the last phases of the trajectory, when contrasted with the low cost incurred, which cannot be reached by any other system, for example, position-sensitive diodes (PSD), which dependably include higher expenses and probably will not be adequate for nonreusable gadgets like artillery munitions. Coordination can be accomplished without requiring extensive transfer of coordinates which is susceptible to mistakes. However, constant lines of sight between the target, laser designator, and the weapon must be maintained. Present day laser-guided weapons are coordinating IMU, GPS, and laser guidance ability, offering high-accuracy, all-climate assault capacity. For instance, in [12], the authors plan a missile target tracker utilizing a filter/correlator dependent on forward-looking infrared sensor estimations. Ground designation and UAV designation may give compelling help to laser targeting. Ground assignment is successful when vertical targets (dividers, entryways, and windows in structures) are locked in while UAVs or other aeronautical devices can exploit the unhindered perspective of the scene. Aside from line-of-sightverification and allocation of codes before the mission, the utilization of SAL does not force facilitating restrictions or complexities while working in good perceivability conditions (day or night), and in this manner, it is reasonable for ad hoc engagements of targets of opportunity and close air support.

Quadrant photodetector is a plate composed of silicon containing two holes over the widths. Along these lines, there are four autonomous and equal photodetectors on the detecting surface, one on every quadrant. The focal point of the detector is known precisely since it is the mechanical convergence of the two-hole lines and is not meant to change with time or temperature. A symmetrical laser impression, or other optical beam fixated on the detector, will create equal current intensities from every one of the four divisions. In the event that the beam moves from the focal point of the detector, the intensities from the four divisions will change and a processing method will provide the coordinate changes with respect to the center of the detector [13]. Accuracy in determining the coordinates of intersection of the beam with the photodetector will decide the key focuses on the navigation and guidance calculations for the terminal stage on a PGM.

Along these lines, generally, a photodetection system can be practically partitioned into two primary parts: sensing and processing. The first stage includes an optic part which is not the aim of this paper; a few references for those sorts of PGM and different applications can be found in [14–17].

In the second stage, the signal postprocessing stage, the sensed signal, i.e., the intensities for every quadrant, is handled to evaluate the spot coordinates and to obtain the required data for the navigation and guidance calculations.

Displacements of the laser footprint center, i.e., spot, on the quadrant detector are not a conspicuous computation as those directions are a function of current produced by every one of the four parts of the photodetector. The standard methodology for the control loop of the servo system works through the difference of the sum of signals coming from the left- and right-side quadrants for horizontal displacement and the difference of the sum of signals coming from the upper- and downside quadrants for vertical displacement [18]. This is very inaccurate, particularly in some cases where relocations from quadrant center are large as demonstrated in [19]. The aim of this paper is to develop new methodologies to correct the mentioned shortcomings in [13, 20–22], where linearity is not achieved but approximated, which is not precise for high dynamics air vehicles, where rapid maneuvering is usually required. An algorithm to reach desired linearity in the four methods and to be applied to guided rockets and projectiles is proposed in this paper.

The purpose of this paper is to obtain a linear method for the laser footprint center calculation, in a semiactive laser quadrant photodetector, by an interpolation algorithm based on the four electrical intensities obtained during simulated shots for an artillery rocket in a set of ballistic flights during its terminal phase. The electrical intensities that a real sensor provides are modeled by a quadrant photodetector mathematical model. It is based on area intersection calculations and assumes that the photocurrent of the four-quadrant photodetectors is proportional to the illuminated area projected on the photosensitive surface, as stated in [13, 20, 21], supposing that reflections, etaloning, schlieren, and other optical effects are handled by the optical design, which is a fair approximation for the aim of this paper, which focuses on signal processing and not on optics. From these intensities, four different processing methods are tested for different spot sizes so as to obtain a correlation algorithm between the real spot center position and the position calculated by the methods. Finally, the flight dynamics rocket model in [1] is employed to compare real and calculated laser footprints in order to select the best algorithm for artillery applications.

1.1. Contributions. The key contribution of this paper is the development of a novel algorithm which improves the precision of spot center determination for a SAL quadrant detector for terminal guidance of artillery rockets. Also, a model for the quadrant detector based on a real-time area intersection algorithm is developed and is compared with data obtained from real measurements under laboratory conditions according to MIL-STD-810 environmental test methods for normative aerospace.

Relevant parameters which influence sensor precision and performance are determined and studied. Also, sensitivity analysis is performed on some of them. It is shown
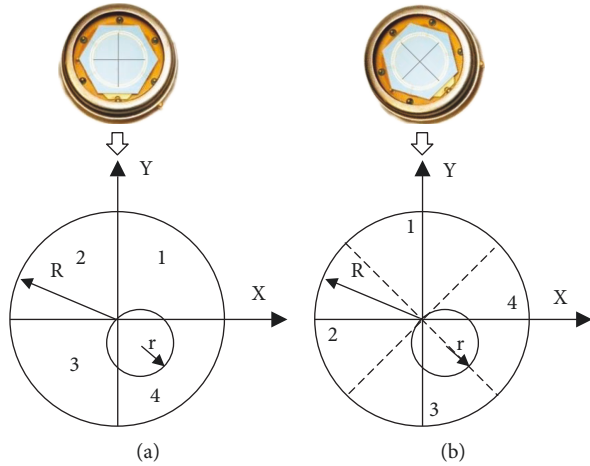
Figure 1: Real sensor and model for standard (a) and cross (b) quadrant detector configuration.

that the transformation of the real to the estimated spot footprint made by the methods is conformal. Based on this, an interpolation algorithm is proposed to obtain predictable performance.

Nonlinear simulations based on ballistic rocket launches are performed to obtain this spot position and compare it to the position obtained from the interpolation algorithms and to demonstrate the applicability of the proposed solution for artillery final flight stage guidance.

The rest of the paper is organized as follows. Section 2 describes first the problem in detail, and secondly, it is devoted to the semiactive laser sensor model. Section 3 describes signal processing algorithms. Section 4 shows simulations results. Section 5 discusses the quality of the results. Finally, in Section 6, some conclusions are drawn.

2. Problem Description

The problem statement for semiactive laser (SAL) terminal guidance usually consists of a soldier or an aircraft enlightening a target with high-energy, short laser pulses in a near-infrared wavelength. Some of the energy from each pulse reflects off the target into the seeker's quadrant detector. By comparing the current measured in each channel of the quadrant detector, the device calculates the position of the reflected intensity within its field of view (FOV). Using this data, the device returns control signals to the projectile's control system to maneuver toward the target [19].

In order to process the signals in each channel, a methodology is needed. The main inputs for processing are the four intensities obtained from each of the four-quadrant photodetectors. According to [13], four methods are suitable to be used for calculating x and y coordinates of the laser footprint or spot center position from those intensities. The quadrant detector panel is placed in "standard configuration" for methods 1 and 2 as shown on the left in Figure 1. For methods 3 and 4, the quadrant detector is placed in a "cross configuration," i.e., rotated 45° as shown on the right in Figure 1. The nominal radius for the quadrant detector is designated as R and for the spot as r. The axes in the quadrant

detector are defined as x and y. Also, quadrants are given by 1, 2, 3, and 4 as shown in Figure 1, which shows two different configurations.

Quadrants are named as indicated in the figure, and current subindexes correspond to each quadrant. The formulas for calculating x and y coordinates for methods 1, 2, 3, and 4 are in equations (1), (2), (3), and (4), respectively. The assumption that these methods are deeply nonlinear is taken, and the results of the centroid position calculation may differ from its real position. The aim of this paper is to provide a correction method for this fact.

$$\begin{pmatrix} x_{\text{calc1}} \\ y_{\text{calc1}} \end{pmatrix} = \begin{pmatrix} \dfrac{(I_1 + I_4) - (I_2 + I_3)}{I_1 + I_2 + I_3 + I_4} \\ \dfrac{(I_1 + I_2) - (I_3 + I_4)}{I_1 + I_2 + I_3 + I_4} \end{pmatrix}, \quad (1)$$

$$\begin{pmatrix} x_{\text{calc2}} \\ y_{\text{calc2}} \end{pmatrix} = \begin{pmatrix} \log \dfrac{I_1 + I_4}{I_2 + I_3} \\ \log \dfrac{I_1 + I_2}{I_3 + I_4} \end{pmatrix}, \quad (2)$$

$$\begin{pmatrix} x_{\text{calc3}} \\ y_{\text{calc3}} \end{pmatrix} = \begin{pmatrix} \dfrac{I_4 - I_2}{I_2 + I_4} \\ \dfrac{I_1 - I_3}{I_1 + I_3} \end{pmatrix}, \quad (3)$$

$$\begin{pmatrix} x_{\text{calc4}} \\ y_{\text{calc4}} \end{pmatrix} = \begin{pmatrix} \log \dfrac{I_4}{I_2} \\ \log \dfrac{I_1}{I_3} \end{pmatrix}. \quad (4)$$

For precise guidance, it is a cornerstone to know, characterize, and limit the discrepancies between the real position of the spot on the quadrant detector and the calculated position using the intensities obtained from the detector. For example, the ratio between the spot and quadrant detector radius, from now spot-detector ratio, influences the reliability of the SAL terminal guidance.

The next subsection develops a model for the SAL sensor to be used in simulations in order to characterize the limitations of the existing methods and to polish their performance.

2.1. Semiactive Laser Sensor Model. The SAL detector is assumed to be a quadrant detector with a spot projected on it. The spot is received into the system from the target. During the development of this research, some tests were made in a black chamber laboratory from the Spanish National Institute for Aerospace Technology (INTA), where foggy condition simulations are possible (according to MIL-STD-810 environmental test methods for normative aerospace), with a real quadrant photodetector device and a Spanish military laser certified by NATO. In more than a hundred tests, the results provided an almost-circular footprint projected on the quadrant photodetector. This fact was the motivation for developing the algorithm discussed in this paper, as in the models, this footprint can be assumed as circular. It is
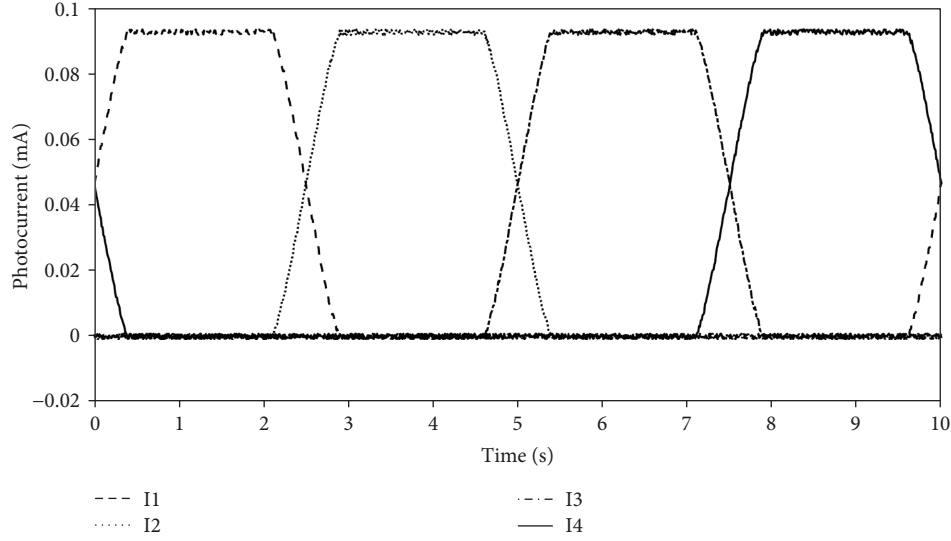
FIGURE 2: Photocurrent versus time registered under laboratory condition tests.
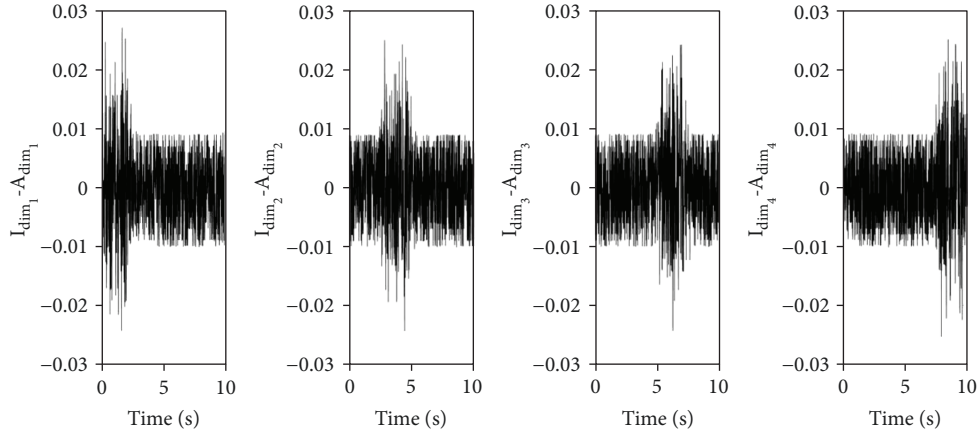

FIGURE 3: Error for nondimensional photocurrent registered under foggy laboratory conditions vs. proposed area method.

also assumed that the current for each quadrant is directly proportional to the area illuminated by the spot in each quadrant [13]. For example, some of the results of these laboratory tests (foggy conditions) for a spot trajectory on a commercial 8 mm laser photodetector, such as the one shown in Figure 1, where the footprint is describing a circumference according to function $x = \sin(0.2\pi \cdot t)$ and $y = \cos(0.2\pi \cdot t)$ for $t = [0, 10]$ s, are shown in Figure 2, as the result of an experiment, where unlike the rest of the paper, the photocurrent profile was not considered to be Gaussian. It must be emphasized that in the rest of the paper, as an assumption [13, 20, 21], the spot photocurrent profile was considered to be Gaussian.

Its comparison against the simulations using the illuminated area method proposed in this paper is shown in Figure 3; in order to express these results, measurements, both for intensities and areas, have been transformed into dimensionless measurements by the following expressions: $I_{\mathrm{dim}_i} = I_i/(I_1 + I_2 + I_3 + I_4)$ and $A_{\mathrm{dim}_i} = A_i/(A_1 + A_2 + A_3 + A_4)$. These results prove the validity of the proposed model for a photodetector based on the area method under some

environmentally unfavorable conditions, as error is always under 1% in relative terms.

2.2. Spot and Photodetector Area Intersection. Assuming that intensities are proportional to illuminated areas [10], the calculation of the area intersection is performed mathematically. The spot is defined as a circle with center $(x_{\mathrm{spot}}, y_{\mathrm{spot}})$ and radius r and the detector as a circle with center $(0, 0)$ and a radius R. Mathematically, they may be expressed as

$$\mathrm{Circ}_{\mathrm{Spot}}\left(x_{\mathrm{spot}}, y_{\mathrm{spot}}, r\right) = \left\{ \left(x_{\mathrm{Circ}_{\mathrm{Spot}}}, y_{\mathrm{Circ}_{\mathrm{Spot}}}\right) \middle| \middle\| \left(x_{\mathrm{spot}}, y_{\mathrm{spot}}\right) \right. \\ \left. - \left(x_{\mathrm{Circ}_{\mathrm{Spot}}}, y_{\mathrm{Circ}_{\mathrm{Spot}}}\right) \middle\| \leq r \right\},$$

(5)

$$\mathrm{Circ}_{\mathrm{Detec}}(0, 0, r) = \left\{ \left(x_{\mathrm{Circ}_{\mathrm{Detec}}}, y_{\mathrm{Circ}_{\mathrm{Detec}}}\right) \middle| \middle\| (0, 0) \right. \\ \left. - \left(x_{\mathrm{Circ}_{\mathrm{Detec}}}, y_{\mathrm{Circ}_{\mathrm{Detec}}}\right) \middle\| \leq R \right\}.$$

(6)

The intersection between the two circles defined by those two circumferences, called Int_1, is calculated as

$$\text{Int}_1 = \text{Circ}_{\text{Spot}} \cap \text{Circ}_{\text{Detec}}. \tag{7}$$

In order to calculate the overlapping area at each quadrant, the following definitions are introduced: top ($\text{TS} = \{x_{\text{TS}}, y_{\text{TS}}\}$), bottom ($\text{BS} = \{x_{\text{BS}}, y_{\text{BS}}\}$), left ($\text{LS} = \{x_{\text{LS}}, y_{\text{LS}}\}$), and right ($\text{RS} = \{x_{\text{RS}}, y_{\text{RS}}\}$) semiplanes. For the "standard configuration," they are defined by $x_{\text{TS}} \in [-R, R]$ and $y_{\text{TS}} \in [0, R]$, $x_{\text{BS}} \in [-R, R]$ and $y_{\text{BS}} \in [-R, 0]$, $x_{\text{LS}} \in [-R, 0]$ and $y_{\text{LS}} \in [-R, R]$, and $x_{\text{RS}} \in [0, R]$ and $y_{\text{RS}} \in [-R, R]$, respectively. For the "cross configuration," the semiplanes are equivalent but applying a rotation of 45°.

Subtraction for each quadrant area calculation is proceeded. For quadrant 1, left and bottom semiplanes are subtracted from Int_1; for quadrant 2, right and bottom semiplanes are subtracted; for quadrant 3, it is proceeded with top and right semiplanes; and for quadrant 4, with top and left semiplanes. Expressions (8), (9), (10), and (11) show the concept for the "standard configuration." Note that intensities are proportional to the illuminated areas and that the proportionality constant is the same for all the quadrants.

$$I_1 \propto A_1 = \text{Int}_1 \cap \text{TS} \cap \text{RS}, \tag{8}$$

$$I_2 \propto A_2 = \text{Int}_1 \cap \text{TS} \cap \text{LS}, \tag{9}$$

$$I_3 \propto A_3 = \text{Int}_1 \cap \text{BS} \cap \text{LS}, \tag{10}$$

$$I_4 \propto A_4 = \text{Int}_1 \cap \text{BS} \cap \text{RS}. \tag{11}$$

Because the calculated spot center depends on the intensities for all the methods, and the intensities are proportional to the illuminated areas [13], it is reasonable to foresee that the spot-detector ratio will be of key importance. The performance of the method will be sensitive to the mentioned spot-detector ratio. Therefore, a set of spot-detector ratios, namely, 0.25, 0.50, 0.75, and 1, will be considered for the remainder of the paper. Note that the assumption that the spot ratio does not vary with the distance of the rocket from the target has been taken, as variations on this magnitude are dependent more likely on the optics of the lens, which has been simplified in this paper.

The obtained dimensionless areas, for the standard configuration, for each of the four photodetectors and sweeping in the domain $[x, y] \in [-1, 1]^2$, are represented in Figure 4. It features spot-detector ratio cases of 0.50, 0.75, and 1.00. On the x and y axes, the coordinates of the spot footprint center are represented, and in the z axis, the illuminated area. For the cross configuration, the results are equivalent but rotated 45°. As may be seen, as the spot-detector ratio increases, the less null illuminated area is obtained, and thus, more information for the processing method is available. However, this does not mean the best approach is the bigger spot-detector ratio as will be shown in the simulations' section.

3. Sensor Signal Processing

This section explains the algorithms employed to process the signals and the interpolation method.

3.1. Spot Center Position Estimation. The line of sight ($\overrightarrow{v_{\text{LOS}}}$) is defined as the line linking the rocket mass center and target. The intersection between $\overrightarrow{v_{\text{LOS}}}$ and the quadrant detector situation plane determines the real spot center.

In order to solve the motion of the ballistic rocket realistically, a nonlinear flight mechanics model for a rocket projectile [1] is employed. The body axis system is defined as follows: x_b pointing forward and contained in the plane of symmetry of the rocket, z_b perpendicular to x_b pointing down and contained in the plane of symmetry of the rocket, and y_b forming a clockwise trihedron as depicted in Figure 5.

The photodetector is contained in a parallel plane to the (z_b, y_b) plane at a distance of d_{panel} from the mass center as shown in Figure 5.

The expressions to determine the coordinates of the real spot center in body axes are in (12); the projections of $d_{\text{panel}}\overrightarrow{v_{\text{LOS}}}$ on each of the body axes are computed to determine the coordinates.

$$\begin{pmatrix} x_{\text{spot}} \\ y_{\text{spot}} \end{pmatrix} = \begin{pmatrix} d_{\text{panel}} \dfrac{\overrightarrow{v_{\text{LOS}}} * \overrightarrow{j_b}}{\overrightarrow{v_{\text{LOS}}} * \overrightarrow{i_b}} \\ d_{\text{panel}} \dfrac{\overrightarrow{v_{\text{LOS}}} * \overrightarrow{k_b}}{\overrightarrow{v_{\text{LOS}}} * \overrightarrow{i_b}} \end{pmatrix}. \tag{12}$$

Figure 6 shows the transformation made from the real spot center to the estimated spot center for each of the methods, i.e., methods 1, 2, 3, and 4. Each subfigure in Figure 6 shows the transformation of a series of real spot center points, given by ($x_{\text{spot}}, y_{\text{spot}}$), and a defining series of circumferences on the quadrant detector: circumferences ranging from 0.1 of the quadrant radius to the quadrant radius itself in intervals of 0.1. Every line of figures shows five different subfigures. The first one, entitled "ideal" represents the ideal circumferences to be transformed by each spot-detector ratio. The rest of the subfigures represent the transformed circumference for each spot-detector ratio, namely, 0.25, 0.50, 0.75, and 1.00.

Analyzing Figure 6, it may be seen that the spot-detector ratios $y_{\text{spot}}/x_{\text{spot}}$ and $y_{\text{calc}_i}/x_{\text{calc}_i}$ for $i = [1, 4]$ are equal, where x_{calc_i} and y_{calc_i} are the transformed coordinates of x_{spot} and y_{spot}, respectively, for at least the locations closer in modulus to the origin than the spot radius inside the quadrant detector. This is the same as saying that angles are maintained for the transformation.

Table 1 shows the coefficient between distances ($d$center) to the quadrant detector center and its radius, given in the first column, and the calculated $\alpha_{\text{calc}_i} = a \tan (y_{\text{calc}_i}/x_{\text{calc}_i})$ for the four methods and for spot-detector ratios of 0.25, 0.50, 0.75, and 1.00, for different $\alpha_{\text{Ideal}} = a \tan (y_{\text{spot}}/x_{\text{spot}})$ given in the second column. Note that some values are
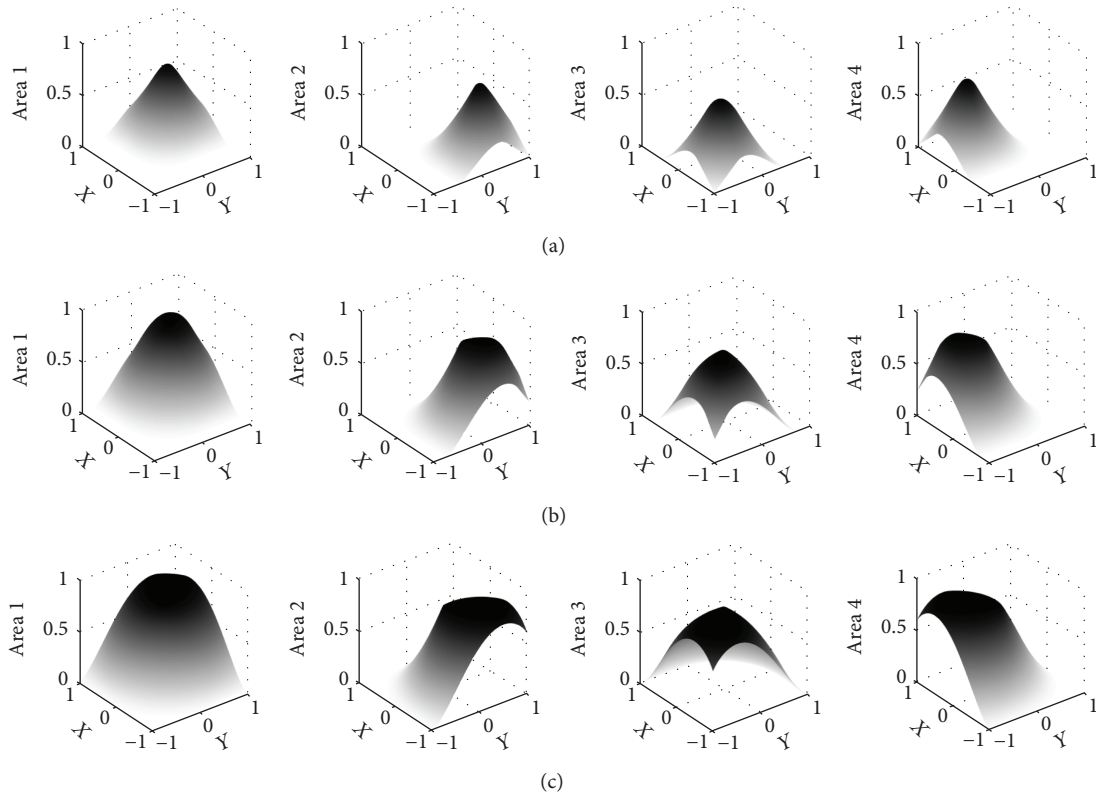
(a)

(b)

(c)

FIGURE 4: Illuminated area for spot-detector ratio of 0.50 (a), 0.75 (b), and 1.00 (c).
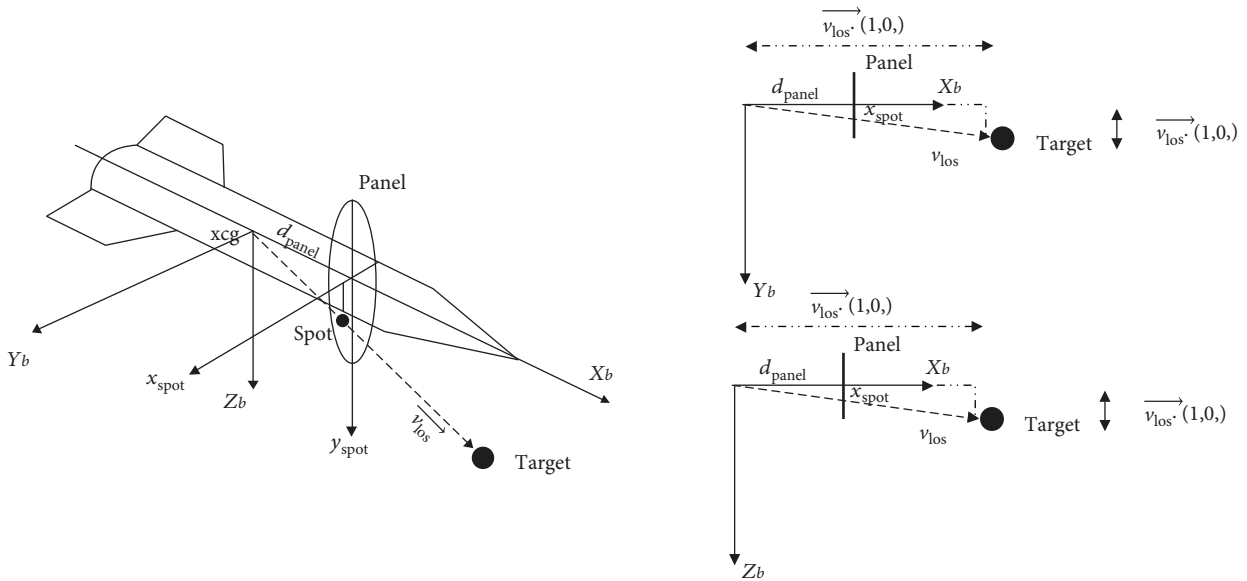
FIGURE 5: Photodetector spot coordinates geometric composition.

"NaN" because the method is dividing by zero; nevertheless, the idea of angles, for at least locations closer in modulus to the origin than the spot radius inside the quadrant detector, being preserved ($\alpha_{\text{Ideal}} = \alpha_{\text{calc}_i}$ for $i = [1, 4]$) remains. It is also demonstrated in this analysis that method 4 preserves angles for more configurations than any other.

3.2. Linear Interpolation. Being the transformation of conformal angles, correlation between real and calculated radial components of the spot center may be estimated using linear interpolation, which has been chosen for its simplicity in implementation but effectiveness in obtaining the desired results. The objective of this interpolation is to avoid the

FIGURE 6: Transformation developed by method 1 (a), method 2 (b), method 3 (c) and method 4 (d).

nonlinear behavior of methods 1, 2, 3, and 4 as it was previously explained.
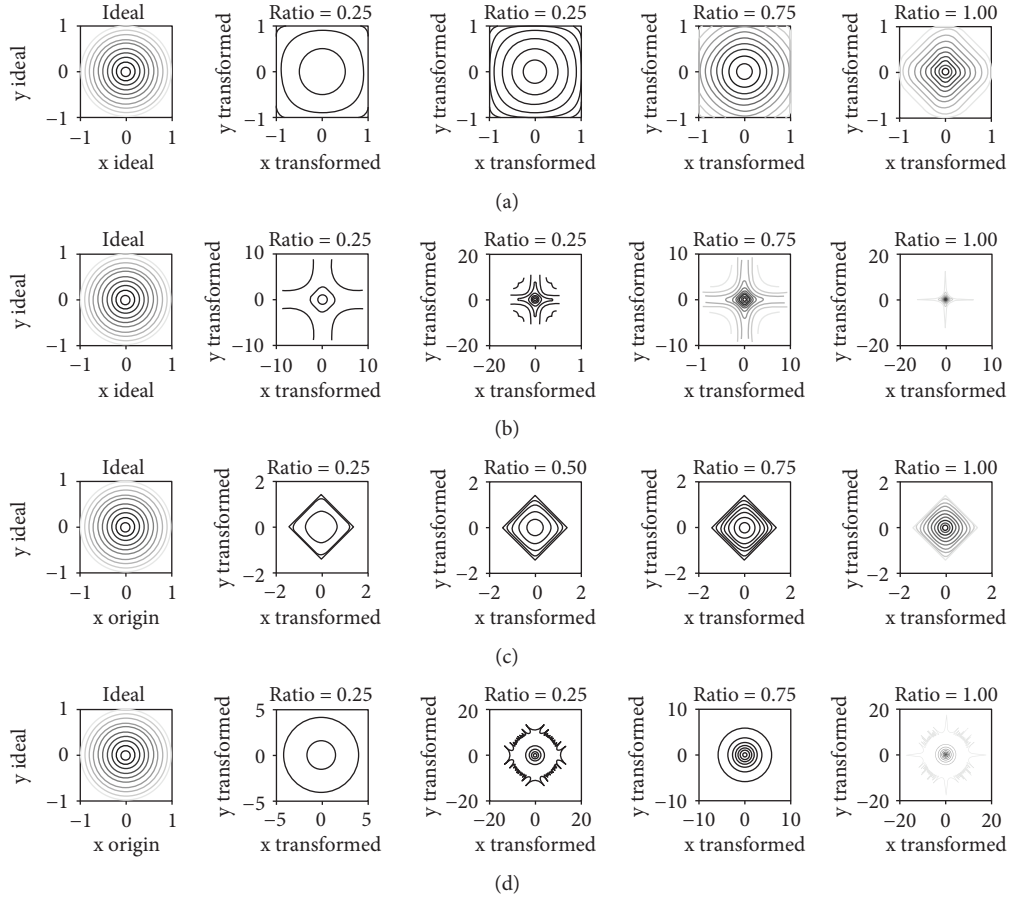
Let ideal radial component be $r_{\text{Ideal}} = \sqrt{x_{\text{spot}}^2 + y_{\text{spot}}^2}$. Based on it and on the calculated radial component $r_{\text{calc}_i} = \sqrt{x_{\text{calc}_i}^2 + y_{\text{calc}_i}^2}$ for $i = [1, 4]$, the interpolated radial component is $r_{\text{Interp}_i} = f(r_{\text{calc}_i})$ for $i = [1, 4]$. Table 2 shows the correlations between the ideal and calculated radial components for the four methods and spot-detector ratios of 0.25, 0.50, 0.75, and 1.00. The first column shows the spot-detector ratio and the second one the radial components (the ideal one in the first row and the calculated ones in the rest of the rows). For example, for a spot-detector ratio of 0.5, ideal radial component of 0.4, and method 4, the calculated radial component is 10.95. Elements in the table with "—" mean saturation.

Therefore, using the values in Table 2 and interpolating, r_{Interp_i} may be estimated for every situation. Interpolated components $(x_{\text{Interp}_i}, y_{\text{Interp}_i})$ for each method may be obtained applying the following transformation:

$$\begin{pmatrix} x_{\text{Interp}_i} \\ y_{\text{Interp}_i} \end{pmatrix} = \begin{pmatrix} r_{\text{Interp}_i} \cos \alpha_{\text{calc}i} \\ r_{\text{Interp}_i} \sin \alpha_{\text{calc}i} \end{pmatrix}, \quad \forall i = [1, 4]. \tag{13}$$

4. Results

MATLAB/Simulink R2015a on a laptop with a 2.6 GHz and 8 GB RAM processor was employed for these simulations.

The algorithm has been tested on a nonlinear flight mechanics artillery rocket model [1], for a set of ballistic shots with launch angles of 15°, 30°, 45°, 60°, and 75°; no wind; and considering a nominal impact point. From this nominal impact point, which is different for different launch angles, the target has been deviated on an 81-point grid with a maximum deviation of 100 m from nominal impact point. A real quadrant detector of 0.08 mm radius has been chosen for the analysis.

This combination of hypotheses results in a campaign of 405 shots for each method and spot-detector ratio: a total amount of 6480 shots have been performed. Due to the huge amount of data obtained, only the results for the shot angles of 30° and 45° with spot-detector ratios of 0.50, 0.75, and 1.00 are shown in Figures 7 and 8, where a comparison between simulated real conditions and proposed algorithm performance is shown. The results for the rest of the simulations show the same performance. Each figure shows four different subfigures, each of them corresponding to a different method. And each of the subfigures shows two different sets of footprints: the simulated real shot results and the interpolated footprints. Each set of footprints

TABLE 1: Relationship angles between ideal and calculated spot center position.

d_{center}/R	Ideal (deg)	Method 1 (deg)				Method 2 (deg)				Method 3 (deg)				Method 4 (deg)			
—	—								Spot-detector ratio								
—	—	0.25	0.50	0.75	1.00	0.25	0.50	0.75	1.00	0.25	0.50	0.75	1.00	0.25	0.50	0.75	1.00
0.1	0.0	0.0	0.0	0.0	0.0	0.0	0.0	0.0	0.0	0.0	0.0	0.0	0.0	0.0	0.0	0.0	0.0
0.1	30.6	31.0	30.7	30.6	30.2	29.8	30.4	30.5	30.1	28.3	30.1	30.4	30.8	30.6	30.6	30.6	30.8
0.1	60.1	59.8	60.0	60.1	60.6	60.9	60.3	60.2	60.6	62.5	60.7	60.4	59.9	60.2	60.1	60.1	59.9
0.1	90.0	90.0	90.0	90.0	90.0	90.0	90.0	90.0	90.0	90.0	90.0	90.0	90.0	90.0	90.0	90.0	90.0
0.2	0.0	0.0	0.0	0.0	0.0	0.0	0.0	0.0	0.0	0.0	0.0	0.0	0.0	0.0	0.0	0.0	0.0
0.2	30.6	32.1	30.9	30.7	29.7	26.7	29.8	30.3	29.7	19.3	28.3	29.6	30.9	30.7	30.6	30.6	31.0
0.2	60.1	58.5	59.8	60.0	61.0	64.1	60.9	60.5	61.1	71.7	62.5	61.1	59.8	60.0	60.2	60.1	59.7
0.2	90.0	90.0	90.0	90.0	90.0	90.0	90.0	90.0	90.0	90.0	90.0	90.0	90.0	90.0	90.0	90.0	90.0
0.3	0.0	0.0	0.0	0.0	0.0	0.0	0.0	0.0	0.0	0.0	0.0	0.0	0.0	NaN	0.0	0.0	0.0
0.3	30.6	36.0	31.4	30.1	29.3	0.0	28.7	29.1	29.1	0.0	25.0	28.0	30.9	NaN	30.5	30.1	31.3
0.3	60.1	54.5	59.3	60.6	61.4	90.0	62.1	61.7	61.6	90.0	65.8	62.8	59.8	NaN	60.2	60.6	59.4
0.3	90.0	90.0	90.0	90.0	90.0	90.0	90.0	90.0	90.0	90.0	90.0	90.0	90.0	NaN	90.0	90.0	90.0
0.4	0.0	0.0	0.0	0.0	0.0	0.0	0.0	0.0	0.0	0.0	0.0	0.0	0.0	NaN	0.0	0.0	0.0
0.4	30.6	42.2	32.2	28.9	28.9	0.0	26.7	27.1	28.6	0.0	19.3	26.0	30.7	NaN	30.7	29.7	31.5
0.4	60.1	48.2	58.5	61.9	61.8	90.0	64.1	63.7	62.2	90.0	71.6	64.9	60.0	NaN	60.0	61.0	59.2
0.4	90.0	90.0	90.0	90.0	90.0	90.0	90.0	90.0	90.0	90.0	90.0	90.0	90.0	NaN	90.0	90.0	90.0
0.5	0.0	0.0	0.0	0.0	0.0	0.0	0.0	0.0	0.0	0.0	0.0	0.0	0.0	NaN	0.0	0.0	0.0
0.5	30.6	45.0	33.4	28.3	28.6	45.0	22.7	25.5	27.9	NaN	9.1	23.9	30.3	NaN	34.2	29.9	31.8
0.5	60.1	45.1	57.2	62.4	62.2	90.0	68.3	65.3	62.9	90.0	81.8	67.0	60.4	NaN	55.7	60.8	58.9
0.5	90.0	90.0	90.0	90.0	90.0	90.0	90.0	90.0	90.0	90.0	90.0	90.0	90.0	NaN	90.0	90.0	90.0
0.6	0.0	0.0	0.0	0.0	0.0	0.0	0.0	0.0	0.0	0.0	0.0	0.0	0.0	NaN	NaN	0.0	0.0
0.6	30.6	45.0	35.2	28.1	28.2	45.0	0.0	23.8	27.1	NaN	0.0	20.6	29.6	NaN	NaN	30.4	32.1
0.6	60.1	45.0	55.3	62.7	62.6	45.0	90.0	67.1	63.7	NaN	90.0	70.3	61.2	NaN	NaN	60.3	58.6
0.6	90.0	90.0	90.0	90.0	90.0	90.0	90.0	90.0	90.0	90.0	90.0	90.0	90.0	NaN	NaN	90.0	90.0
0.7	0.0	0.0	0.0	0.0	0.0	0.0	0.0	0.0	0.0	0.0	0.0	0.0	0.0	NaN	NaN	0.0	0.0
0.7	30.6	45.0	38.1	28.1	27.9	45.0	0.0	21.3	26.1	NaN	0.0	15.0	28.3	NaN	NaN	32.0	32.4
0.7	60.1	45.0	52.5	62.7	62.9	45.0	90.0	69.5	64.7	NaN	90.0	75.9	62.5	NaN	NaN	58.7	58.2
0.7	90.0	90.0	90.0	90.0	90.0	90.0	90.0	90.0	90.0	90.0	90.0	90.0	90.0	NaN	NaN	90.0	90.0
0.8	0.0	0.0	0.0	0.0	0.0	0.0	0.0	0.0	0.0	0.0	0.0	0.0	0.0	NaN	NaN	NaN	0.0
0.8	30.6	45.0	40.9	28.5	27.6	45.0	0.0	17.2	24.9	NaN	0.0	5.7	26.1	NaN	NaN	45.0	32.9
0.8	45.0	45.0	45.0	45.0	45.0	45.0	45.0	45.0	45.0	NaN	NaN	45.0	45.0	NaN	NaN	45.0	45.0
0.8	60.1	45.0	49.7	62.2	63.2	45.0	90.0	73.8	66.0	NaN	90.0	85.1	64.8	NaN	NaN	45.0	57.8
0.8	90.0	90.0	90.0	90.0	90.0	90.0	90.0	90.0	90.0	90.0	90.0	90.0	90.0	NaN	NaN	NaN	90.0
0.9	0.0	0.0	0.0	0.0	0.0	0.0	0.0	0.0	0.0	0.0	0.0	0.0	0.0	NaN	NaN	NaN	0.0
0.9	30.6	45.0	43.5	30.5	27.4	45.0	0.0	0.0	23.2	NaN	0.0	0.0	22.4	NaN	NaN	NaN	33.7
0.9	45.0	45.0	45.0	45.0	45.0	45.0	45.0	45.0	45.0	NaN	NaN	45.0	45.0	NaN	NaN	45.0	45.0
0.9	60.1	45.0	47.0	60.1	63.5	45.0	90.0	90.0	67.7	NaN	90.0	90.0	68.6	NaN	NaN	NaN	57.0
0.9	90.0	90.0	90.0	90.0	90.0	90.0	90.0	90.0	90.0	90.0	90.0	90.0	90.0	NaN	NaN	NaN	90.0
1.0	0.0	0.0	0.0	0.0	0.0	0.0	0.0	0.0	0.0	0.0	0.0	0.0	0.0	NaN	NaN	NaN	NaN
1.0	30.6	45.0	45.0	33.8	27.3	45.0	0.0	0.0	20.7	NaN	0.0	0.0	15.4	NaN	NaN	NaN	37.9
1.0	45.0	45.0	45.0	45.0	45.0	45.0	45.0	45.0	45.0	NaN	NaN	45.0	45.0	NaN	NaN	45.0	45.0
1.0	60.1	45.0	45.1	56.8	63.6	45.0	90.0	90.0	70.4	NaN	90.0	90.0	75.8	NaN	NaN	NaN	53.0
1.0	90.0	90.0	90.0	90.0	90.0	90.0	90.0	90.0	90.0	90.0	90.0	90.0	90.0	NaN	NaN	NaN	NaN

is composed of 9 footprints. From the 81 available footprints, only 9 are shown (in order to clarify the graphs): the one corresponding to the center of the grid, the ones corresponding to the vertexes of the grid, and the ones in the middle of the lines that join the vertexes. The rest of the information is not shown because the outcome is

TABLE 2: Correlations between ideal and calculated radial components.

Spot-detector ratio	r_{Ideal}	0.1	0.2	0.3	0.4	0.5	0.6	0.7	0.8	0.9	1.0
0.25	r_{calc1}	0.50	0.89	—	—	—	—	—	—	—	—
0.25	r_{calc2}	1.09	2.89	—	—	—	—	—	—	—	—
0.25	r_{calc3}	0.70	1.27	—	—	—	—	—	—	—	—
0.25	r_{calc4}	1.54	4.09	—	—	—	—	—	—	—	—
0.50	r_{calc1}	0.25	0.50	0.72	0.90	1.00	—	—	—	—	—
0.50	r_{calc2}	0.52	1.09	1.80	2.90	7.74	—	—	—	—	—
0.50	r_{calc3}	0.36	0.70	1.01	1.27	1.41	—	—	—	—	—
0.50	r_{calc4}	0.73	1.54	2.54	4.10	10.95	—	—	—	—	—
0.75	r_{calc1}	0.17	0.34	0.49	0.61	0.74	0.86	0.97	—	—	—
0.75	r_{calc2}	0.34	0.70	1.06	1.42	1.89	2.60	4.16	—	—	—
0.75	r_{calc3}	0.24	0.47	0.69	0.87	1.04	1.22	1.37	—	—	—
0.75	r_{calc4}	0.48	0.99	1.50	2.01	2.67	3.68	5.88	—	—	—
1.00	r_{calc1}	0.07	0.14	0.23	0.32	0.43	0.54	0.67	0.79	0.92	—
1.00	r_{calc2}	0.14	0.29	0.47	0.67	0.92	1.22	1.61	2.16	3.14	—
1.00	r_{calc3}	0.10	0.20	0.32	0.46	0.61	0.77	0.94	1.12	1.30	—
1.00	r_{calc4}	0.19	0.41	0.66	0.95	1.30	1.72	2.27	3.06	4.43	—

— Real footprint
- - - Interpolated footprint
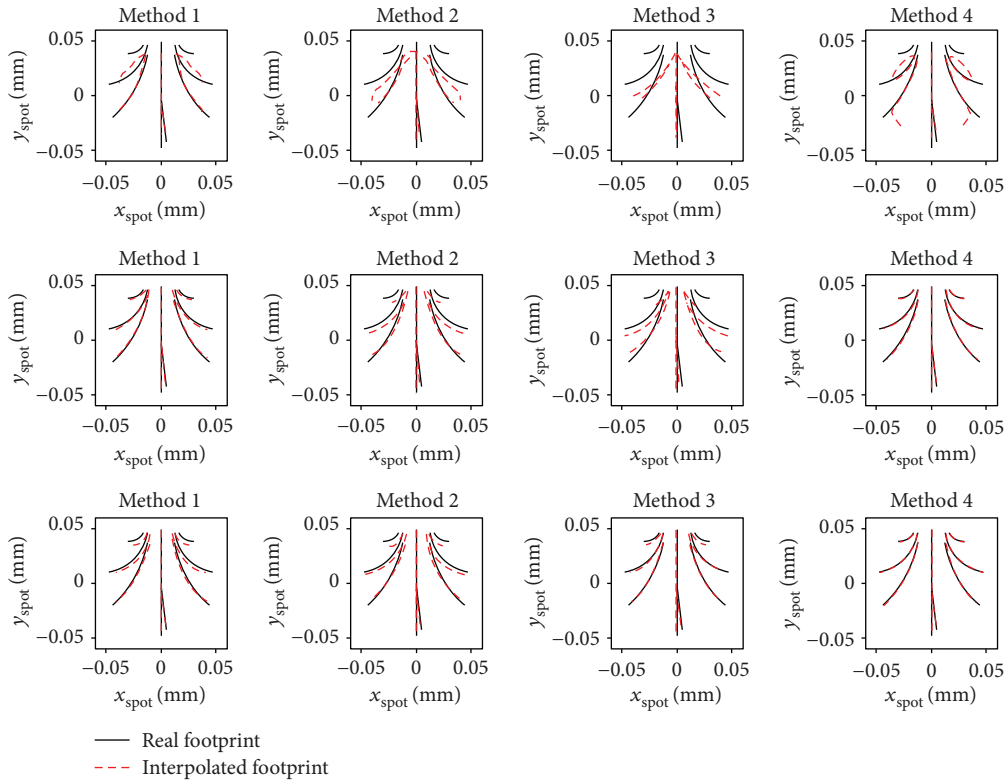
FIGURE 7: Detector footprint for a shot angle of 30° with a spot-detector ratio of 0.50 (top), 0.75 (middle), and 1.00 (bottom).

the same. Note that the best performance is obtained when both footprints, namely, simulated real and interpolated, are as similar as possible. This is achieved for most of the tested cases in this paper. However, the results in [13, 20] show that linearity is lost especially on the outer parts of the quadrant photodetector.

5. Discussion

In order to quantify the error made by each of the methods, the total quadratic error ($QE_i^{\gamma,sqr}$) is calculated in (14). This error depends on the shot launch angle (γ), spot-detector ratio (sqr), and method (i).
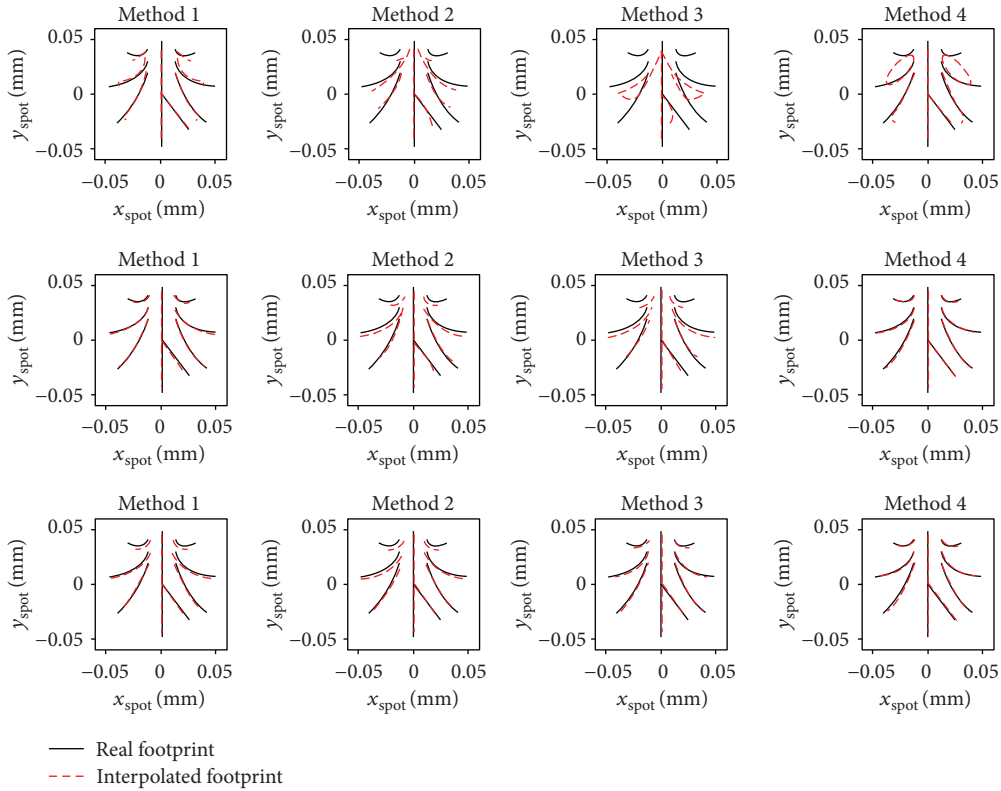
— Real footprint
- - - Interpolated footprint

FIGURE 8: Detector footprint for a shot angle of $45°$ with a spot-detector ratio of 0.50 (top), 0.75 (middle), and 1.00 (bottom).
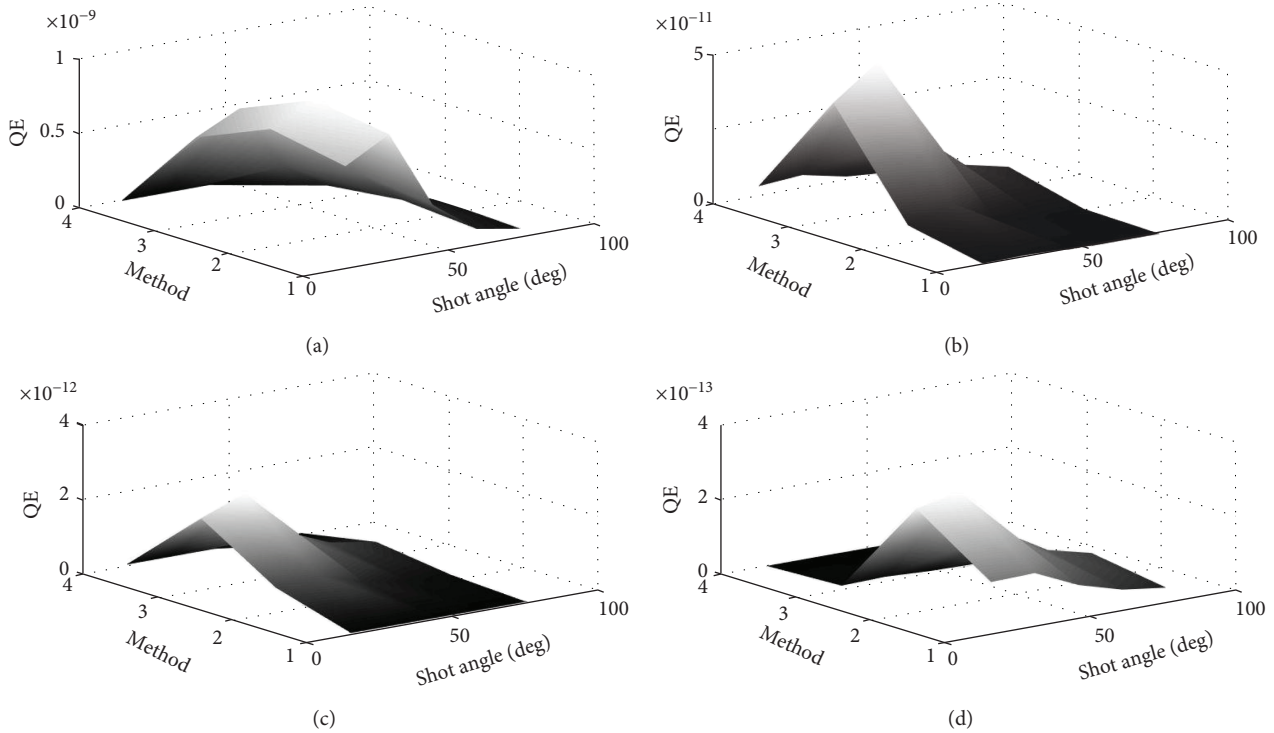

(a)

(b)

(c)

(d)

FIGURE 9: Quadratic error for different combinations of shot angles and methods, for each spot-detector ratio ((a) 0.25, (b) 0.50, (c) 0.75, (d) 1.00).

$$\mathrm{QE}_i^{\gamma,\mathrm{sqr}} = \sum_{j=1}^{81} \oint \sqrt{\left(x_{\mathrm{Interp}_i} - x_{\mathrm{spot}}\right)^2 + \left(y_{\mathrm{Interp}_i} - y_{\mathrm{spot}}\right)^2}\, d\sigma_j. \tag{14}$$

Figure 9 shows $\mathrm{QE}_i^{\gamma,\mathrm{sqr}}$. Each of the subplots show the spot-detector ratio. The y axis shows the method used, and the x axis shows each launch shot angle. Finally, the z axis represents the error as calculated in (14). Obviously, the smaller the quadratic error is, the better is the used approach. Therefore, method 4 with a spot-detector ratio of 0.75 is the best combination to be used for this application. Note that Figures 7 and 8 confirm this aspect: footprints are almost the same for method 4 and a spot-detector ratio of 0.75.

6. Conclusions

A novel approach which improves the precision of spot center determination for a SAL quadrant detector for terminal guidance of artillery rockets has been proposed. Relevant parameters which influence sensor precision and performance have been determined, and sensitivity analysis on some of them has been performed.

It is found that the transformation of the real to the estimated spot footprint made by the method is conformal. Based on this, an interpolation method is proposed to get improved performance.

From the sensitivity analysis, it has been shown that the combination of a logarithmic approach based on intensity ratios and spot-detector ratio of 0.75 is the most accurate approach.

Nonlinear simulations based on ballistic rocket launches are performed to obtain simulated real spot position and compare it to the position obtained by the proposed approach.

This precise spot center coordinate calculation approach may be employed in several applications such as the determination of the line of sight between the rocket and target during the terminal phase.

Data Availability

The data used to support the findings of this study are included within the article.

Conflicts of Interest

The authors declare that there is no conflict of interest regarding the publication of this paper.

Acknowledgments

References

[1] R. de Celis, L. Cadarso, and J. Sanchez, "Guidance and control for high dynamic rotating artillery rockets," *Aerospace Science and Technology*, vol. 64, pp. 204–212, 2017.

[2] N. Barbour and G. Schmidt, "Inertial sensor technology trends," *IEEE Sensors Journal*, vol. 1, no. 4, pp. 332–339, 2001.

[3] P. Gurfil, "Robust guidance for electro-optical missiles," *IEEE Transactions on Aerospace and Electronic Systems*, vol. 39, no. 2, pp. 450–461, 2003.

[4] I. R. Manchester, A. V. Savkin, and F. A. Faruqi, "Method for optical-flow-based precision missile guidance," *IEEE Transactions on Aerospace and Electronic Systems*, vol. 44, no. 3, pp. 835–851, 2008.

[5] S. Kim and K. T. Kim, "Adjacent infrared multitarget detection using robust background estimation," *Journal of Sensors*, vol. 2016, Article ID 7279081, 10 pages, 2016.

[6] Y. Wang, G. P. Hu, and H. Zhou, "Group targets tracking using multiple models GGIW-CPHD based on best-fitting Gaussian approximation and strong tracking filter," *Journal of Sensors*, vol. 2016, Article ID 7294907, 13 pages, 2016.

[7] D. Hantke, H. Philipp, G. Sparrer, and J. Tschirnich, "Precision measurement on position-sensitive photodetectors," *Measurement*, vol. 7, no. 4, pp. 153–156, 1989.

[8] J. Q. Qian, Y. Cui, and P. Xu, "The study for measuring rotor speed and direction with quadrant photoelectric detector," *Measurement*, vol. 41, no. 6, pp. 626–630, 2008.

[9] Z. Zhang, Y. Dong, F. Ni, M. Jin, and H. Liu, "A method for measurement of absolute angular position and application in a novel electromagnetic encoder system," *Journal of Sensors*, vol. 2015, Article ID 503852, 10 pages, 2015.

[10] K. Holldack, W. B. Peatman, and T. Schroeter, "Vertical photon beam position measurement at bending magnets using lateral diodes," *The Review of Scientific Instruments*, vol. 66, no. 2, pp. 1889–1891, 1995.

[11] R. de Celis and L. Cadarso, "Attitude determination algorithms through accelerometers, GNSS sensors, and gravity vector estimator," *International Journal of Aerospace Engineering*, vol. 2018, Article ID 5394057, 14 pages, 2018.

[12] P. S. Maybeck, T. D. Herrera, and R. J. Evans, "Target tracking using infrared measurements and laser illumination," *IEEE Transactions on Aerospace and Electronic Systems*, vol. 30, no. 3, pp. 758–768, 1994.

[13] C. B. Shen, B. G. Sun, T. J. Ma, P. Lu, S. F. Lin, and X. H. Wang, "Research of signal-processing methods in four-quadrant photodetector," in *2008 International Conference on Electrical Machines and Systems*, pp. 917–919, Wuhan, China, October 2008.

[14] C. A. I. Yi and X. Hu, "State of the art and future trend of detectors for infrared imaging seekers," *Infrared and Laser Engineering*, vol. 1, 2006.

[15] W. Kuang-Biao, "Status quo, key technology and development of laser guided weapon," *Infrared and Laser Engineering*, vol. 5, 2007.

[16] R. M. Sullivan, "A history of semi-active laser dome and window materials," in *Proceedings of SPIE 9453, Window and*

Dome Technologies and Materials XIV, Baltimore, MD, USA, 2015International Society for Optics and Photonics.

[17] Y. Tian, H. Yan, G. Sun et al., "Semi-active laser/millimetre wave beam combiner design and test," *IET Microwaves, Antennas & Propagation*, vol. 9, no. 8, pp. 830–836, 2015.

[18] S. Donati, C. Y. Chen, and C. C. Yang, "Uncertainty of positioning and displacement measurements in quantum and thermal regimes," *IEEE Transactions on Instrumentation and Measurement*, vol. 56, no. 5, pp. 1658–1665, 2007.

[19] V. N. Singh, "Laser power distribution for detection performance in laser system," in *Proceedings of Fifth International Conference on Soft Computing for Problem Solving 2015*, pp. 665–671, Springer, Singapore, 2016.

[20] C. F. Kuang, Q. B. Feng, J. Y. Feng, and B. Liu, "Analyzing characteristic of the four-quadrant detector applied to laser alignment," *Optical Technique*, vol. 4, 2004.

[21] F. Longling, "Simple analysis of signal-processing skill for four-quadrant opto-electronic detective system," *Optical Technology*, vol. 3, 1995.

[22] J. C. Xing and C. Tian, "Measurement method and system of parameters of quadrantal detector," *Infrared Technology*, vol. 26, no. 2, pp. 33–36, 2004.